Oxygen vacancies and interfaces enhancing photocatalytic hydrogen production in mesoporous CNT/TiO$_2$ hybrids

[Alicia Moya](#)[a], [Alexey Cherevan](#)[b], [Silvia Marchesan](#)[c], [Paul Gebhardt](#)[b], [Maurizio Prato](#)[c], [Dominik Eder](#)[b, ,], [Juan J. Vilatela](#)[a, ,]

Show more

Highlights

- Mesoporous TiO$_2$/CNT hybrid were synthesised through sol–gel and electrospinning.

- O vacancies and interfaces are the key during structural evolution of the hybrids.

- Interfaces TiO$_2$/TiO$_2$ and TiO$_2$/CNT enhance photocatalytic activity.

- Use as photocatalyst, they produce 14 times more H$_2$ than nanoparticles of TiO$_2$.

Abstract

We demonstrate a unique route towards hierarchical assemblies of mesoporous TiO$_2$ and CNT/TiO$_2$ photocatalysts by a combination of electrospinning and sol–gel methods. The resulting materials exhibit a mesoporous network of highly crystalline, well-connected inorganic nanocrystals with an order of magnitude higher photocatalytic activity than individualised TiO$_2$ nanoparticles. The *in-situ* combination of small amounts of MWCNTs

with TiO$_2$ to form an electrospun CNT/TiO$_2$ hybrid further enhanced the oxide photoactivity considerably, reaching hydrogen evolution rates of 1218 μmol/h in water splitting in the presence of sacrificial reagents under UV irradiation. We also discuss the effect of oxygen vacancies on the oxide crystallisation and phase transformation. These vacancies lead to inter-bandgap states and a lower flat band potential that facilitates the photocatalytic process.

Graphical abstract
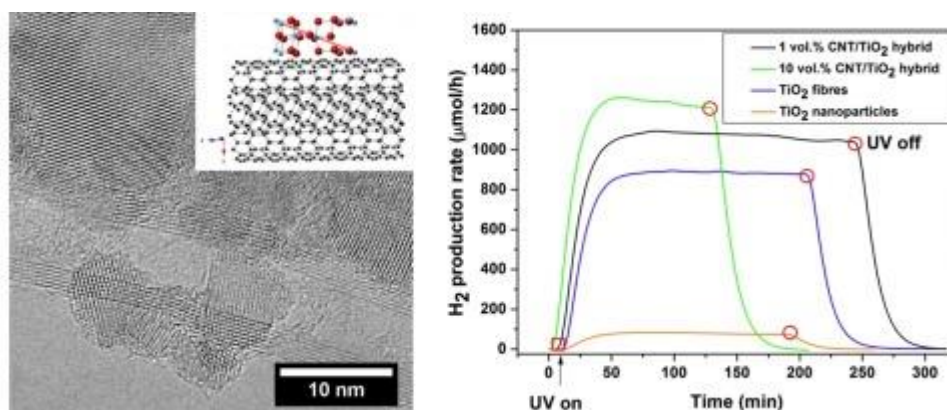
1. Introduction

The unique features of nanomaterials have made them particularly attractive in the field of photocatalysis. In addition to the benefits of a large surface-to-volume ratio that facilitates the catalytic conversion of adsorbed reaction species [1], and shorter charge transfer distances [2], nanoparticles often exhibit optical properties distinct from the bulk. Importantly, these can induce a larger absorption cross-section, and thus an extension of the absorption range of visible light [3].

The available library of nanostructured catalysts has also evidenced that the combination of two nanomaterials represents a powerful strategy to gain deeper insights into the various processes taking place during photocatalysis and, ultimately, to increase the efficiency of energy conversion processes. A simple approach is the mechanical mixing of different components into a composite. However, their hybridisation into one structure, for example by growing *in-situ* one nanomaterial in presence of the other, is a more powerful method that allows for more consistent and reproducible structures of improved photocatalytic properties [4]. In contrast with simple composites, such hybrids offer the key benefits of intimate interfaces, namely (1) facilitation of charge/energy transfer and (2) increased lifetime of charge carriers through spatial separation of photoexcited electron-hole pairs. As a result, appropriately engineered hybrids can display increased photocatalytic efficiency, amongst other attributes [5]. Engineering of such interfaces, for example through bottom-up fabrication from molecular precursors, can further improve

their performance and also evolve new material structures through epitaxial growth [6], heat-sink effects [7], the stabilisation of unusual phases [8] and core-shell nanoparticles [9].

Among the many different classes of hybrids, those based on a semiconductor and a nanocarbon, such as carbon nanotubes (CNT) or graphene, have received vast attention [10], [11], [12] and [13]. Nanocarbons are chemically robust, while also easily functionalised for further processing and for the tailoring of the interfacial interaction with the semiconducting phase [14]. They can act as electron acceptors/donors and have a high intrinsic mobility (>100,000 cm^2/Vs) in the absence of defects [15] and [16]. With the aim of increased efficiency in photocatalysis, nanocarbons have been hybridised with a wide range of inorganics such as metal oxides, oxynitrides or zeolites [8]. TiO_2-graphene hybrids, for example, have been shown to reach 2–3 times higher photocatalytic activities compared with the inorganic catalyst [17], [18] and [19]. Recently, Cherevan et al. have reported Ta_2O_5-CNT hybrids capable of an activity that is 35 times higher relative to the individual inorganic compound; this was achieved by controlling the interface and the morphology of the nanocarbon-inorganic hybrids to maximise synergism for photocatalytic hydrogen production [20].

An underlying principle in these hybrid materials is the importance of the interface between nanocarbon and inorganic phase. The inorganic component is typically grown on, or in the presence of, the nanocarbon to obtain a tight interface that represents an electronic junction to favour charge transfer between the two components. Amongst the possible synthetic routes to produce such a structure, the combination of sol–gel and electrospinning is particularly attractive. In this method, a polymer used as vehicle for spinning keeps the sol units agglutinated in close proximity, and, upon annealing, it produces a crystalline porous structure [21] and [22]. When spun in the presence of nanocarbons, the resulting structure is an inorganic matrix hosting a small fraction of nanocarbon [23], which, by being embedded in it, shares a large interface with the inorganic component. An additional interest in this technique arises from the high photocatalytic activity reported for the pure inorganic fibres. Used as photocatalysts *via* water splitting with sacrificial reagents, pure TiO_2 electrospun fibres have shown activity as high as 830 µmol/h. While this is largely a consequence of the relatively high porosity of these fibres and the predominance of the anatase phase, recent reports also suggest a longer charge lifetime through an intrinsic electron-hole separation mechanism across the interconnected inorganic nanocrystals in the fibre [24].

This paper sets out to study the structure and photocatalytic properties of electrospun CNT/TiO_2 hybrids, first by looking at the complex structural evolution of the material during synthesis, then by comparing their structure, morphology and porosity with pure TiO_2 fibres and pure TiO_2 nanoparticles, and finally by relating their optoelectronic properties and photocatalytic activity for hydrogen production through sacrificial water splitting under UV irradiation. These materials serve as a test system to gain insight into more general properties of hybrids, thus providing tools for the rational design and synthesis of new nanostructured hybrids with improved catalytic performance in sustainable energy

applications, such as water splitting, water purification, photoelectrochemistry and photovoltaic devices.

2. Experimental

2.1. Materials

High purity MWCNTs were supplied by Thomas Swan Co., Ltd. All other chemicals were purchased from Sigma–Aldrich.

2.2. Sample preparation

2.2.1. CNT functionalisation

MWCNTs with diameters of 10 ± 3 nm were rendered dispersible through oxidative surface functionalisation (by ultrasonication-assisted oxidation at RT for 5 h with a 3:1 mixture of concentrated H_2SO_4/HNO_3, creating carboxyl acid groups, followed by extensive washings in water and methanol) [25]. The oxidised tubes displayed 8.0 ± 2.0 wt.% functionalisation as established by TGA, corresponding to a theoretical content of 1.8 ± 0.5mmol COOH/g CNTs. The presence of carboxyl groups was confirmed by FT-IR analysis (Fig. S1). After the treatment, their lengths were considerably shortened, with the majority of the nanotubes having a length between 100 and 500 nm, and only a very minor percentage (<5%) exceeding 1 micron. As a result, the material could be easily dispersed as individual nanotubes, as observed by TEM imaging (Fig. S2), for further processing. Importantly, in contrast with the pristine MWCNTs, the oxidised nanotubes (ox-CNT) yielded stable dispersions in polar solvents, allowing for further processing such as electrospinning.

2.2.2. Preparation of TiO_2 and hybrid nanofibers

TiO_2 and TiO_2/CNT nanofibres were synthesised by a combination of sol–gel and electrospinning. The solution used for electrospinning contained the polymer, TiO_2 precursor (alcoholic solution of titanium ethoxide with controlled pH) and CNTs for the hybrids production. A polyvinyl pyrrolidone (PVP) solution in ethanol (10 wt.%) was stirred and then mixed with the alcoholic solution of titanium ethoxide (63.5 wt.%) and a few drops of acetic acid to catalyse the TiO_2 sol–gel reaction. In the case of hybrids, CNT dispersions in ethanol were added in different volume fractions (0.35–10 vol.%) to the solution mixture and vigorously stirred to obtain a uniform dispersion. The solution was placed in a syringe and fed into an electrospinning set-up (Nanon 01A, MECC Co., Ltd.). Electrospinning was performed at an applied potential of 18 kV and a flow rate of 2 mL/h. Fibres were collected over aluminium foil placed 10 cm below the tip. After electrospinning, samples were annealed at 400 °C for 150 min in air to remove the polymer. Crystallisation of titania was performed in Ar atmosphere to prevent CNT oxidation. A wide range of annealing temperatures (500–800 °C) was used to study the phase transformation and to produce samples of deliberately small or large anatase to rutile ratio. Most samples subjected to photocatalytic tests (including those in Fig. 8) were crystallised at 500 °C for 1 h under Ar

atmosphere to reduce possible effects of the annealing process, and thus to enable a more direct comparison between samples.
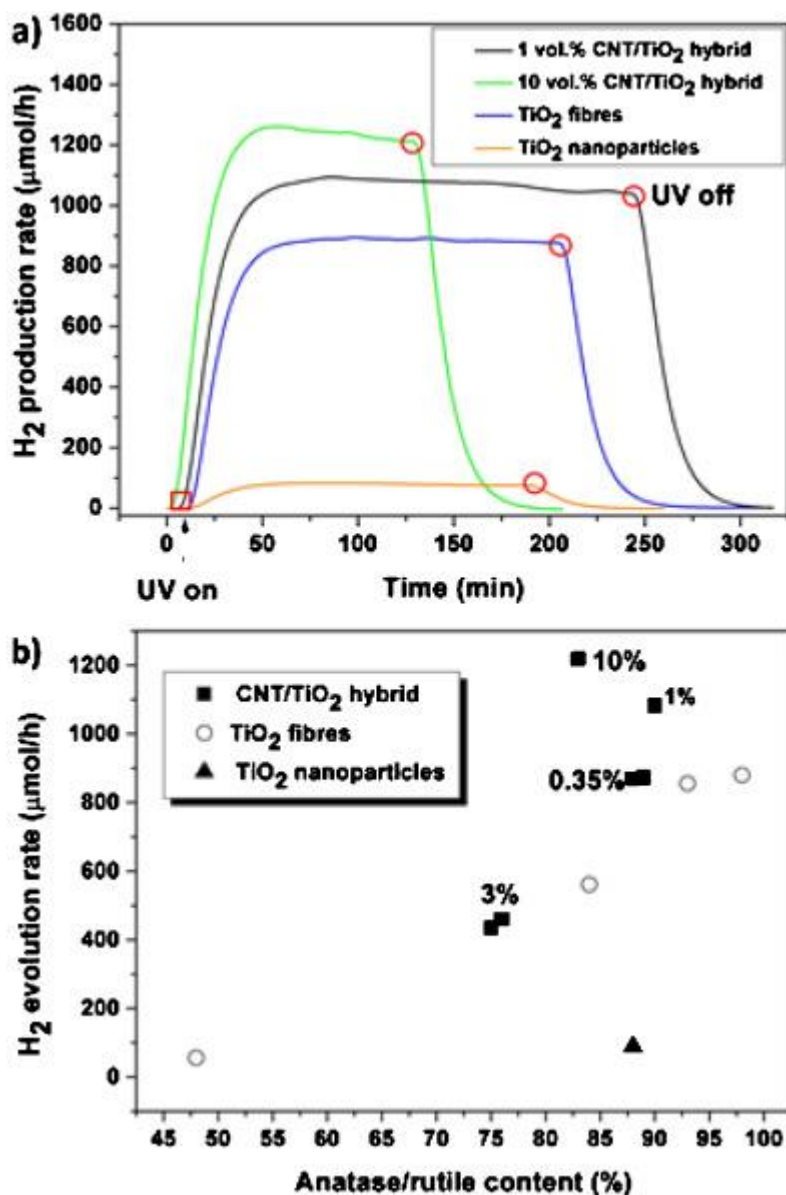

Fig. 8.

Photocatalytic activity of 1 and 10 vol.% CNT/TiO$_2$ hybrid and TiO$_2$ reference samples (mesoporous and nanoparticles). (a) Continuous H$_2$ monitoring during a typical photocatalytic test. (b) Photocatalytic activity as function of the anatase/rutile content.

Figure options

2.2.3. Preparation of TiO$_2$ nanoparticles

TiO$_2$ nanoparticles were prepared by standard sol–gel method. An acidic solution of titanium ethoxide (3 mL) and absolute ethanol (10 mL) were vigorously stirred at 80 °C during a day. After the ethanol evaporation, a TiO$_2$ yellowish powder was obtained, which

was still amorphous. Heat treatment at 500 °C for 1 h produces crystalline anatase TiO_2 nanoparticles.

2.3. Structural and physical characterisation

Morphological and structural analysis of the fibres were done using a scanning electron microscope at 4–10 keV (SEM, EVO MA15, Zeiss Model) and high resolution transmission electron microscope (HRTEM, JEOL JEM 3000F) operating at 300 kV. Phase analysis was performed using X-Ray Diffraction (XRD), X́Pert MD Analytical. From XRD patterns, average crystal size was calculated using Scherrer's equation [26] and the anatase/rutile ratio according to Spurr's equation [27]. Small-angle X-ray scattering (SAXS) measurements were performed at the NCD beamline of Alba using a wavelength of 1 Å and taking around 50 2D individual 0.1s-exposure patterns. For each sample 50 patterns were averaged and then azimuthally integrated to convert to 1D intensities. Raman spectroscopy was performed with a Jasco NRS-5100 spectrometer using a laser of 532 nm of wavelength at 5.3 mW. Adsorption–desorption isotherms were carried out on Micrometrics ASAP 2010 at 77 K with N_2 as adsorbate. Specific surface area (according to BET) and porosity (according to BJH) were determined assuming 0.162 nm^2 as the nitrogen molecule area. FT-IT measurements were carried out using a PerkinElmer 2000 spectrometer. The FT-IR spectra were acquired with KBr discs under transmission mode, using the instrument Spectrum software at a resolution of 4 cm^{-1}. The scanned wavenumber range was from 4000 to 400 cm^{-1}. Thermogravimetric analysis (TGA) were performed using TA Instruments TGA Q500 with a ramp of 10 °C/min under nitrogen gas from 100 to 800 °C. Ultraviolet–visible Diffuse Reflectance Spectroscopy (UV–vis DRS). Absorption studies were obtained in Lambda 1050, PerkinElmer in the range of 250–800 nm. $BaSO_4$ was used as standard sample. The indirect bandgap energy was calculated from the intercept of the tangents to the curve of $(\alpha E_{photon})^{1/2}$ vs E_{photon}. Photoluminescence Spectroscopy. Emission spectra of solid samples were measured in a Fluorescence Spectrometer PerkinElmer LS 55, using 280 nm as excitation wavelength and a cut-off filter at 350 nm. X-ray Photoelectron Spectroscopy (XPS) data were collected in a SPECS GmbH electron spectroscopy system provided with a PHOIBOS 150 9MCD analyser.

2.4. Electrochemical impedance spectroscopy (EIS)

Electrochemical tests were performed in a three-electrode cell with a platinum counter electrode and Ag/AgCl reference electrode. The area of the TiO_2 electrode was 2 cm^2 and the electrolyte was 0.1 M Na_2SO_4 adjusted at pH 2 with sulphuric acid. Electrode impedance measurements were carried out with a SP-200 Bio-Logic potentiostat with AC signal of 10 mV amplitude in the frequency range 10 kHz–10 mHz and applied bias from 0.6 V to −1 V vs Ag/AgCl reference electrode.

2.5. Photocatalytic experiments

Photocatalytic hydrogen production experiments were performed in a flow-type cylindrical reactor with a top cap made of quartz glass for top-irradiation. A UV–vis light source (Lumatec) equipped with 200 W super pressure Hg lamp was used to deliver light in the wavelength range of 240–500 nm by means of an optical fibre. X-Stream gas analyser (Emerson Process Management) was used to monitor evolved H_2 on-line. The reactor was continuously purged with Ar 99.998% to trap the products and deliver them to the detector. In a typical experiment, photocatalyst (30 mg) were dispersed in 200 ml reaction mixture (50:50 water:methanol) to yield a homogeneous slurry. Pt nanoparticles (0.5 wt.%) were *in-situ* photodeposited by adding the respective amount of H_2PtCl_6 solution into the reaction media prior to the irradiation. Collected data corresponds to continuous sampling of H_2 production over time.

3. Results and discussion

The synthesis of nanocarbon/TiO_2 hybrids through annealing of electrospun fibres constitutes a very interesting new approach that is substantially different from the production of nanoparticles of TiO_2 using conventional methods, such as standard sol–gel. Electrospun hybrids have a more complex structure, arising mainly from the following features of the synthetic process: (a) the addition of a large content of a suitable polymer agglutinates the sol and the nanocarbons in the sample before calcination; (b) the removal of the polymer, *i.e.* by annealing the fibres in air, which initiates the densification of the sol into a porous network of interconnected TiO_2 nanoparticles, and (c) the presence of the nanocarbon hybridised with TiO_2 creates additional interfaces. The presence of nanocarbons further implies that the conditions for annealing at high temperatures, such as above 500 °C required for the crystallisation of TiO_2 into anatase, require the use of inert gases in order to avoid oxidation of the CNT [28].

3.1. Electrospun hybrid structure

A schematic of a hybrid fibre produced under our choice of synthetic conditions and examples of corresponding electron micrographs are presented in Fig. 1. The as-electrospun samples consist of long fibres with diameters of ~800 nm that typically contain around 50 wt.% polymer along with the TiO_2 gel and the embedded nanocarbon in the case of the hybrid fibres. Removal of the polymer induces densification of the gel, simultaneously forming a continuous mesoporous inorganic network. This results in a reduction of fibre diameter to a few hundred nanometres (Fig. 1b). The choice of polymer is crucial; fibres that are electrospun using polyvinyl acetate (PVAc), for example, form only short "spindles" when are annealed at similar temperatures [29], presumably due to decomposition of PVAc occurring at lower temperature compared to PVP. The final materials produced after polymer removal (400 °C in air) and crystallisation (500 °C in Ar) preserve the fibrillar structure but with a high porosity, as shown in Fig. 1c. Higher magnification TEM micrographs (Fig. 1d) reveal the structure of interconnected.
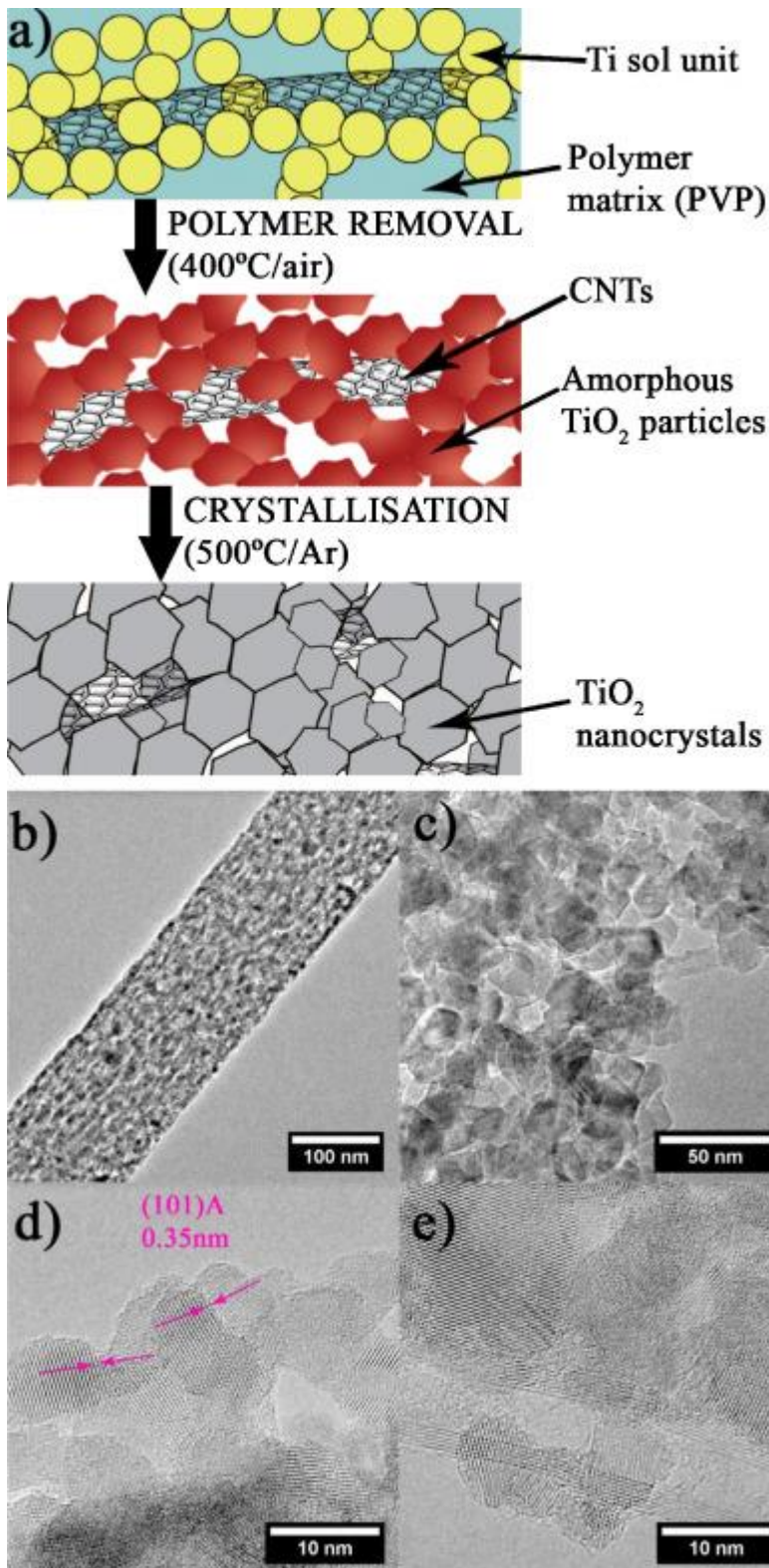
Fig. 1.

(a) Schematic of a hybrid fibre throughout the synthetic process: (1) Electrospinning: CNT and Ti precursor are embedded in a polymer fibre matrix (blue background); (2) Polymer removal: densification of the sol units forming TiO_2/CNT fibres of connected TiO_2 amorphous particles; (3) Crystallisation: produces mesoporous fibres of interconnected nanocrystallites of titania hybridised

with the CNT. (b–e) Transmission electron micrographs of the mesopororous structure formed by interconnection of titania nanocrystals; (d) shows the (1 0 1) lattice fringe of anatase and the tight interface between anatase nanocrystals and (e) a CNT hybridised with TiO_2 nanocrystals.

Figure options

TiO_2 nanocrystals forming a large number of interfaces in the form of defined grain boundaries. Successful hybridisation through *in-situ* synthesis is also confirmed by the presence of TiO_2 in close proximity to the CNTs, as shown in Fig. 1e.

From Fig. 1 it is clear that such fibres, whether as hybrid or pure inorganic fibres, are very different from individual nanoparticles typically used as catalysts. Thus, as a necessary tool towards understanding of the structure/properties of the final electrospun CNT/TiO_2 hybrids, throughout this work we also include the comparison between mesoporous and nanoparticle TiO_2 (*i.e.* without CNTs) and their differences in terms of pore structure, surface area, phase composition, and photocatalytic activity.

Gas adsorption measurements, presented in Fig. 2, confirm the mesoporosity of the electrospun fibres. The BJH pore size distribution of the electrospun materials obtained from the adsorption branch is wider compared to a control sample of TiO_2 nanoparticles produced by sol–gel (*i.e.* no electrospinning), with an average pore radius of 2.1, 7.3 and 5.6 nm for TiO_2 nanoparticles, TiO_2 fibres and hybrid fibres, respectively. Further characterisation by SAXS indicates that the annealed fibres exhibit a fractal structure in the range 10–60 nm corresponding to the type observed in multiparticle diffusion-limited aggregates and linear swollen polymers [30] (see Fig. S3), whereas the control samples of TiO_2 nanoparticles appears as a smooth surface under SAXS in this range.
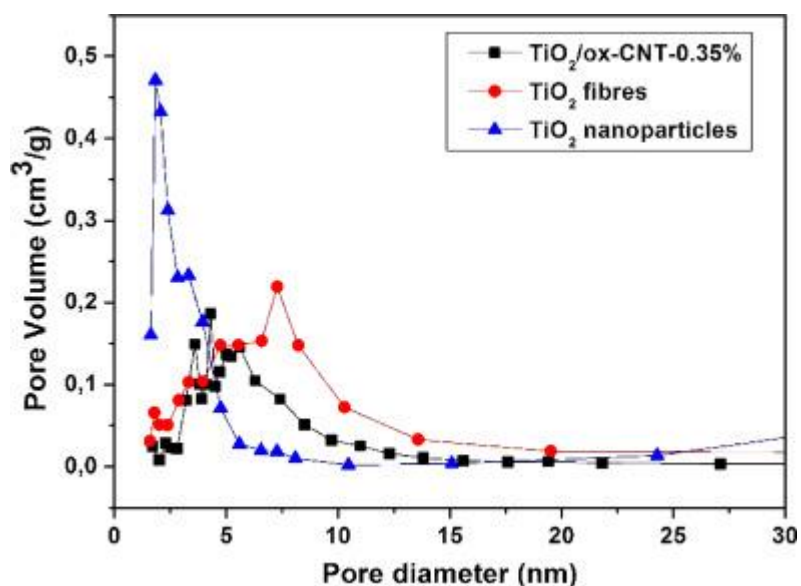

Fig. 2.

A comparison of BJH pore size distribution of electrospun fibres of pure TiO_2 and TiO_2/CNT hybrid and TiO_2 nanoparticles obtained from adsorption branch.

Fig. 3 shows the Raman spectra for electrospun TiO_2 fibres, TiO_2/CNT hybrid fibres and TiO_2 nanoparticles for comparison. All the samples exhibit the five active modes of TiO_2, corresponding to 144 (E_g), 198 (E_g), 397 (A_{1g}), 516 (A_{1g} or B_{1g}) and 639 (E_g) cm^{-1} in bulk anatase. The first two modes present a blue shift, higher for the fibres (6 cm^{-1}) compared to the particles (3 cm^{-1}) and increasing with CNT content (7 and 10 cm^{-1} for 1 and 10 vol.% of CNTs). While this blue shift is usually related to phonon confinement in small particle sizes [31], we note that the average crystal size of our samples is similar (11–15 nm). Furthermore, it is not clear that such confinement would be present in nanocrystals joined as a mesoporous structure rather than individualised. Instead we attribute the shift in Raman modes to O vacancies due to the sensitivity of the Eg mode to O—O interactions [32]. These defects are likely to involve sharing of oxygen at the interfaces between TiO_2 nanocrystals and the TiO_2/CNT interface. As such, they can be expected to create inter-bandgap energy levels in the system, similar to those observed in bicontinuous mesoporous TiO_2 self-assembled from block copolymers [33]. Photoluminescence (PL) observed in the range 2–3 eV corresponding to emission of excitons associated to surface oxygen vacancies and defects [34], [35], [36] and [37] confirms this to be the case (see Fig. S4). Furthermore, because no partial reduction of Ti^{4+} to Ti^{3+} was found in XPS (Fig. S5), such levels would be closer to the conduction band edge and would lead to an n-type semiconductor (later confirmed by impedance).
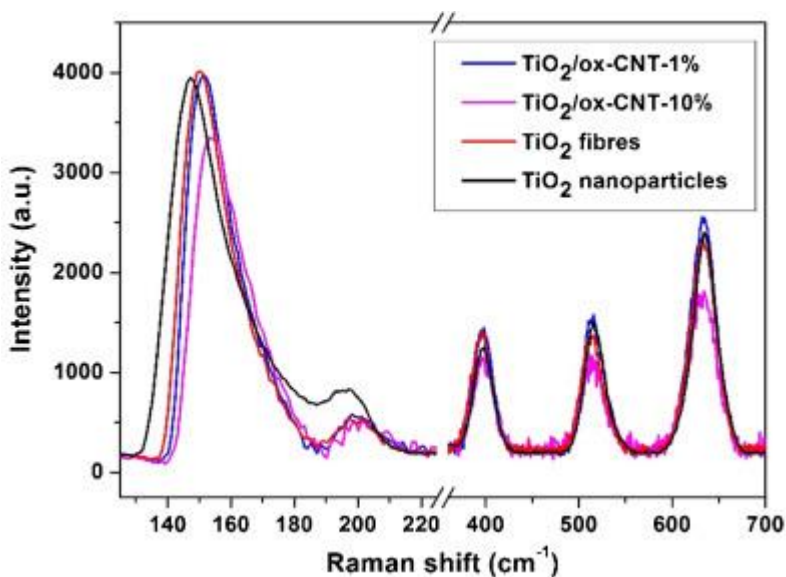

Fig. 3.

Raman spectra of electrospun fibres of pure TiO_2 and hybrids with 1 and 10 vol.% of CNTs. TiO_2 nanoparticles included for comparison. The blue shift in the E_g modes for the electrospun samples corresponds to O vacancies.

From the results above, it is apparent that the electrospun fibres resemble a high porosity continuous network of interconnected nanocrystals of non-stoichiometric anatase TiO_2,

very different from individualised nanoparticles typically used as catalysts, and somewhat similar to nanocrystalline porous electrodes produced by sintering of inorganic nanoparticles slurries [38]. The observed structure evolves through the confluence of three inter-dependent processes, namely (1) sol–gel, (2) sintering and polymer removal and (3) crystallisation. Due to their effect on hybrid structure and photocatalytic activity, some aspects of the synthetic process are discussed in more detail below.

3.2. Crystallisation into a mesoporous structure

The starting point in the formation of the continuous mesoporous structure is the accelerated crystallisation of the sol units confined in the electrospun polymer. The XRD patterns in Fig. 4 show that electrospun fibres already present the typical fingerprint diffractions of crystalline titania after polymer removal at 400 °C in air, such as a well-defined (1 0 1) reflection and other less intense peaks attributed to the anatase phase (A). In contrast, a control sample of TiO_2 nanoparticles produced by standard sol–gel (*i.e.* without polymer and electrospinning) and annealed under identical conditions appears significantly less crystalline under XRD (Fig. 4). The difference arises from the increased density of the gel-network in the electrospun material that favours sintering and crystallisation of the fibre, although higher annealing temperature (500 °C) is still required to complete the crystallisation process and to produce a more efficient catalyst.
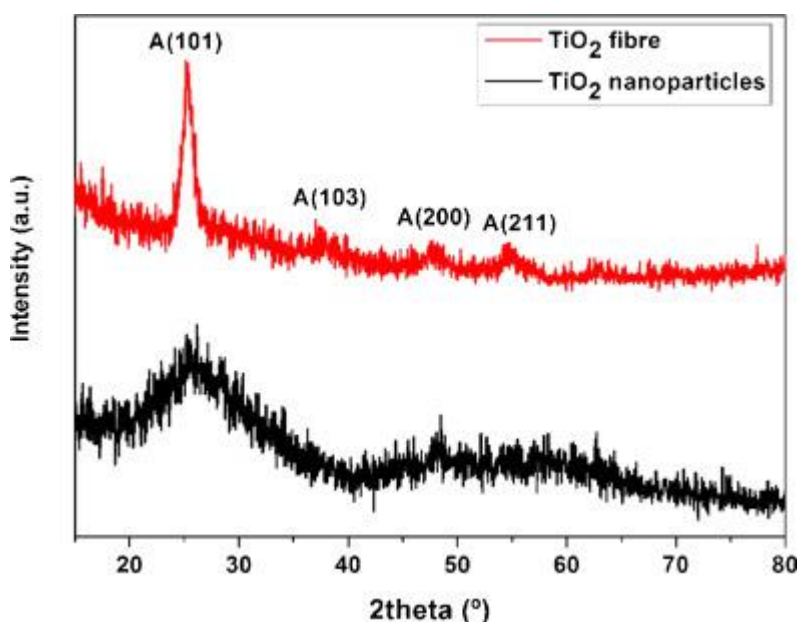

Fig. 4.

XRD patterns of TiO_2 fibres and nanoparticles produced under the same annealing conditions for 150 min in air at 400 °C. The TiO_2 fibre crystallises from a continuous sol structure rather than individual particles, resulting in accelerated crystallisation as shown by the anatase peaks in XRD.

Figure options

The crystallisation process at 500 °C produces a network of interconnected titania nanocrystals that evolves into a mesoporous fibre with interfaces. Such interface also accelerates the anatase-rutile phase transformation compared to that of individualised nanoparticles. We observe rutile (R) in electrospun samples annealed at temperatures as low as 500 °C, whereas isolated TiO_2 nanoparticles of similar crystal size experience the phase transformation when they are annealed at higher temperatures (see Fig. S6). This occurs because of the lower activation energy for the formation of rutile nuclei at the boundary between anatase crystals [39] and [40]. In our mesoporous materials, such interface corresponds to the abundant interfaces between nanocrystals, as opposed to the limited contact in nanoparticle samples produced by standard sol–gel methods. We can approximate the relative size of interfacial area between TiO_2 nanocrystals as the difference between geometric surface minus effective exposed surface measured by BET. Calculating the geometric surface assuming spherical crystals with diameter equal to the average crystal size determined by XRD (150 m^2/g), and measured values of BET surface (41.4 m^2/g), the nanocrystal interface comes out as 109 m^2/g (Fig. S7).

3.3. The role of the inert atmosphere

The crystallisation annealing process is carried out in inert atmosphere in order to preserve the CNTs which, although stable *per se* in air up to 600 °C, could be catalytically oxidised by reduction of the metal oxide in contact with them [28]. We find the crystallisation process to be strongly affected by the inert atmosphere, particularly the onset of anatase-rutile transformation. Fig. 5 presents the evolution of XRD patterns of samples annealed under high flow of air (a) and Ar (b), respectively. It clearly shows that the absence of oxygen promotes an earlier crystallisation into anatase and also transformation to rutile, which starts below 500 °C in Ar, compared to 650 °C in air. Raman spectroscopy (Fig. 5c) further indicates that the fraction of rutile/anatase increases with increased Ar gas flow during annealing, suggesting that the diffusion of gas molecules in the electrospun membrane array of porous fibres is an important parameter for hybrid synthesis.

a)

Air

(110)R

(101)A

14/86

92/8

100/0

100/0

Intensity (a.u.)

2theta (º)

400ºC
500ºC
650ºC
800ºC

b)

Ar

R

0/100

49/51

84/16

A

100/0

Intensity (a.u.)

2theta (º)

800ºC
650ºC
500ºC
400ºC

c)

No flow
High flow

A

R

R

A

A

A

A

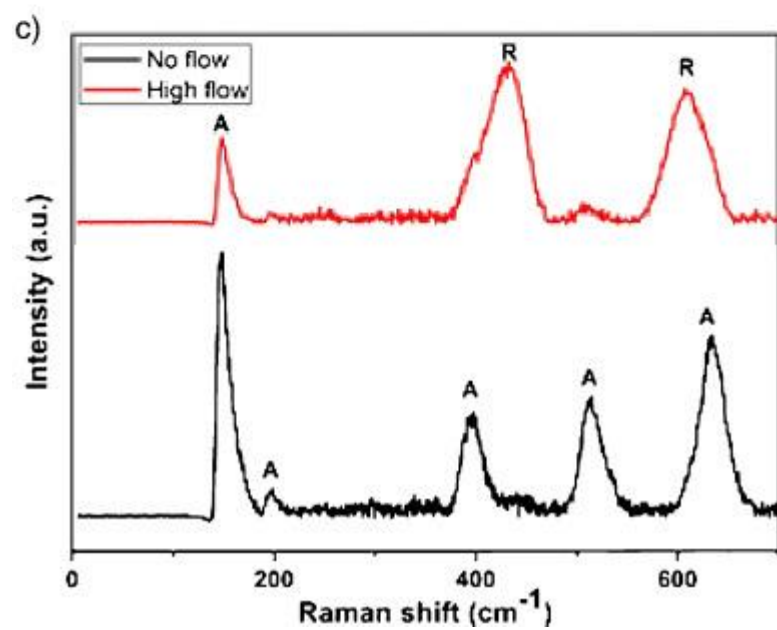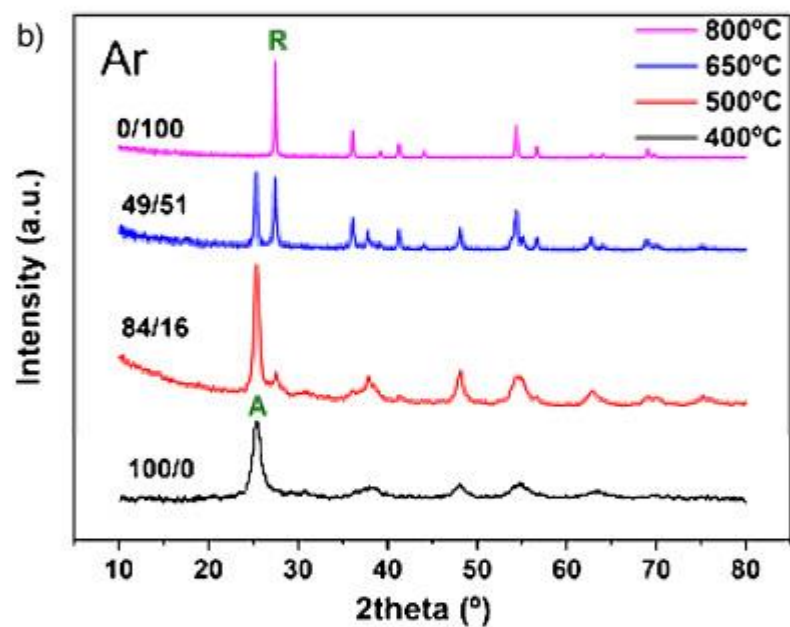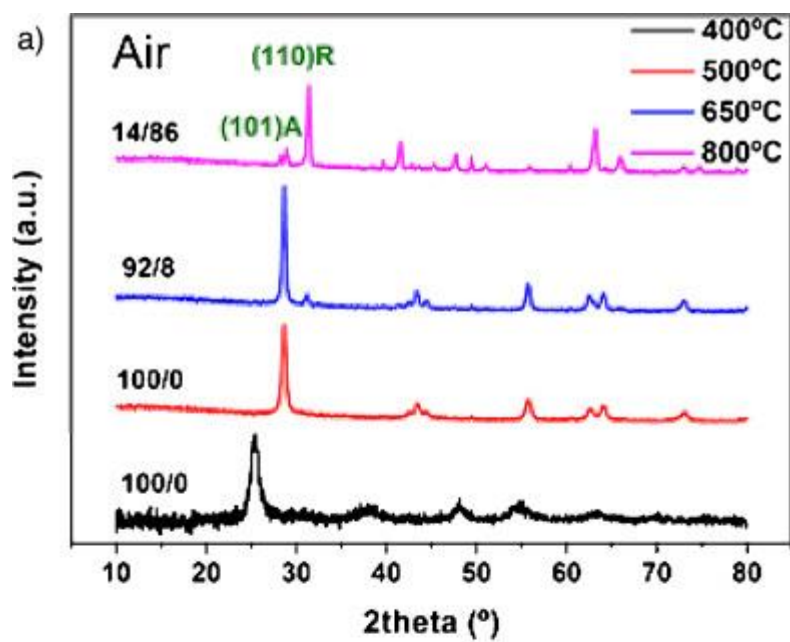Intensity (a.u.)

Raman shift (cm⁻¹)

Fig. 5.

XRD patterns and Raman spectra showing the effect of annealing atmosphere on phase composition. In air (a) the A–R transformation starts around 650 °C, whereas in Ar (b) rutile is detected as low as 500 °C. Raman spectroscopy (c) shows high Ar flow rates to increase rutile content.

The early formation of rutile in inert atmosphere annealing is a consequence of the formation of a partially reduced oxide, where O vacancies act as defects that favour repositioning of Ti and O atoms in the rearrangement of Ti—O octahedral from anatase to rutile. These vacancies and defects can be formed by reduction of the oxide through annealing in reducing atmospheres (*e.g.* CO_2/H_2) [41] or by incomplete oxide synthesis in an inert atmosphere (*e.g.* in Ar) [7]. They effectively lower the energy barrier for the phase transformation and accelerate the process kinetics [42]. The overall net effect is facilitation of the phase transformation, while limiting particle coarsening. Importantly, the key factor for this mechanism to occur is the fact that the anatase nanocrystals share common interfaces, where the octahedral rearrangement takes place. Finally, our tests for photocatalytic hydrogen production shown that the annealing process in Ar at 500 °C present an optimum rutile amount that benefit the photocatalytic process (see section 3.5).

3.4. The CNT-TiO$_2$ interface

The other relevant interface in these systems is the one between CNTs and TiO$_2$. Our HRTEM observations indicate that the separation between TiO$_2$ crystals and CNTs is below 1 nm and confirm the successful hybridisation of the CNTs through *in-situ* growth of the inorganic compound [43]. The close proximity between the two nanostructures is depicted in Fig. 6, which shows a CNT/TiO$_2$ nanocrystal interface. The observed lattice fringes correspond to the (1 0 1) planes of TiO$_2$ which are at 30° to the (0 0 2) planes of the CNT. The molecular model in the inset shows the corresponding crystallographic orientation of the two phases where their interface is formed by the (1 0 1) TiO$_2$ and (0 0 2) CNT planes. This crystal arrangement is the most prominent, although other interfaces have also been observed.
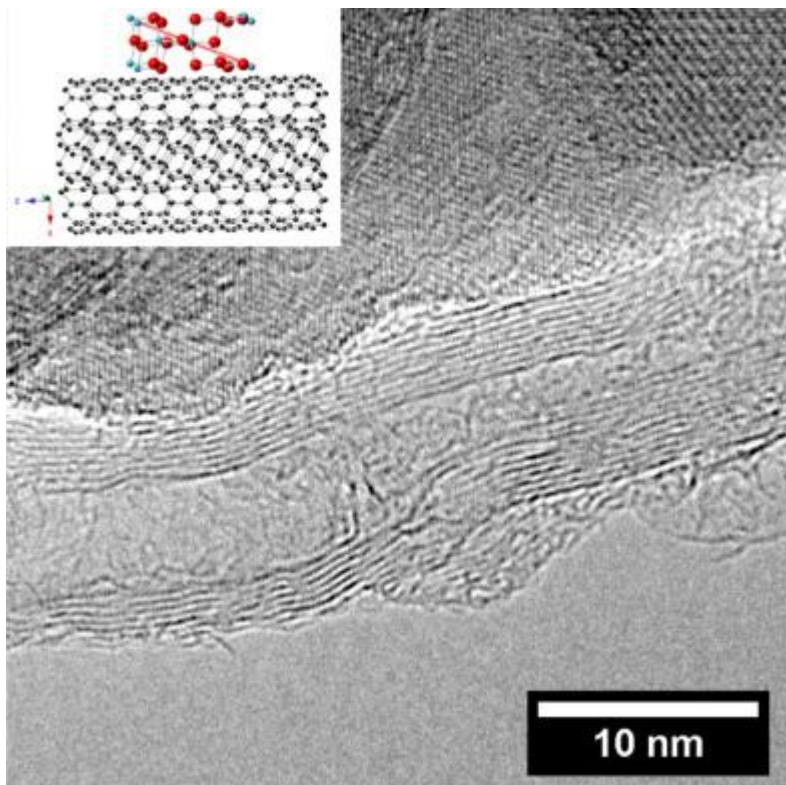
Fig. 6.

The interface of a CNT/TiO$_2$ in hybrids is characterised by the close proximity of the two phases. HRTEM showing the CNT surface supporting TiO$_2$ nanocrystal, with the interface corresponding to (1 0 1)TiO$_2$/(002)CNT (inset).

Figure options

Through FT-IR spectroscopy we have further characterised the interface in the hybrids. Fig. 7 presents FT-IR spectra of a hybrid with high amount of functionalised CNTs (40 vol.%) to increase signal intensity from interfacial FT-IR modes. Spectra of the functionalised CNTs, and of a sample of TiO$_2$ produced by an identical electrospinning and annealing process, are also included for reference. The signals in the region 1630–1400 cm^{-1} in the hybrid confirm the presence of CNTs and indicate that the polymer removal process does not produce apparent damage to the nanotubes. By contrast, as expected, the annealing process in Ar leads to the loss of the CNT functional groups associated with the original oxidative functionalisation (especially the C$=$O signal at 1730 cm^{-1}, and also the asymmetric and symmetric C$-$H stretchings at 2930 cm^{-1} and 2860 cm^{-1} are notably reduced, see Fig. S8). More importantly, the hybrid presents signals at 1160, 1090 and 1030 cm^{-1} which could correspond to rocking and stretching modes previously assigned to Ti$-$O$-$C [44] and [45]. CNTs also present weak signals arising from C$-$O vibrations in this region; however, in the hybrid IR spectrum, we can rule out such peak assignment to the CNT themselves, in light of the expected intensity relative to the CNT fingerprint, and of the absence of the C$=$O signal in the hybrid IR spectrum.
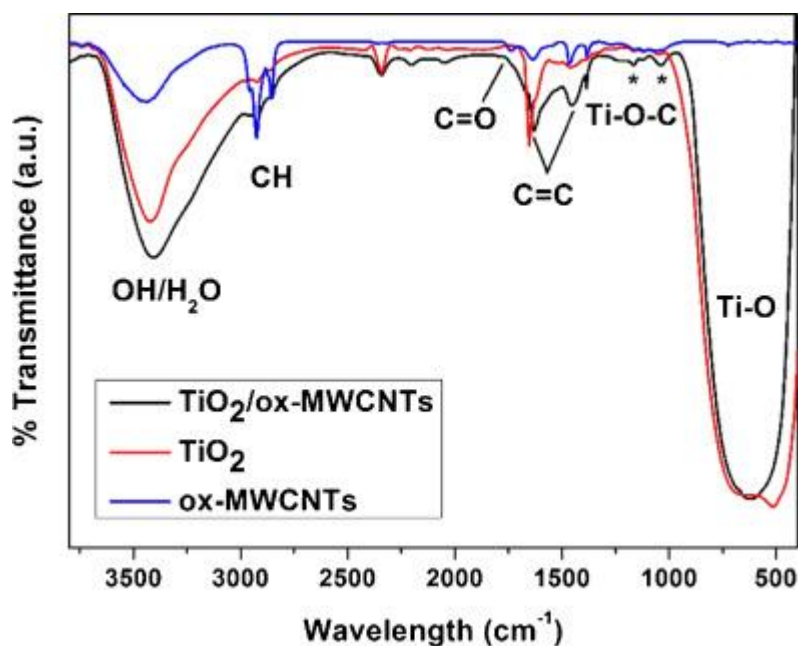
Fig. 7.

FT-IR spectra of a hybrid with oxidised CNTs (a) and reference samples of the oxidised CNTs (b) and pure TiO_2 fibre (c). The spectra confirm the presence of CNTs in the hybrid and show a Ti—O—C bond (*) at the TiO_2/CNT interface.

[Figure options]

The FT-IR data point to the formation of a covalent Ti—O—C bond at the TiO_2/CNT interface. Such covalent bond, formed during the *in-situ* growth process, could facilitate interfacial electron transfer and enhance the photocatalytic activity of the material through spatial charge separation.

3.5. Photocatalytic activity

We have studied the photocatalytic activity for hydrogen production of these hybrids and we have compared it with reference samples (*i.e.* electrospun TiO_2 nanofibres and TiO_2 nanoparticles). The tests were carried out under UV irradiation using Pt as a co-catalyst, and applying a gas detection system that enables continuous monitoring of H_2 evolution. Characterisation of the photocatalyst after the hydrogen production was performed to evaluate possible changes in the morphology of the fibres and to the dispersion of the Pt nanoparticles in the fibre (see Fig. S9).

Fig. 8a presents typical results obtained with a 1 and 10 vol.% CNT/TiO_2 hybrid, a sample of pure TiO_2 fibres that was produced under identical conditions except for the addition of nanocarbon, and a sample of TiO_2 nanoparticles produced by standard sol–gel. All of them were crystallised at 500 °C for 1 h under Ar gas flow. The plot shows a rapid activation of the catalysts upon illumination, reaching their stable activity only a few minutes after switching on the lamp. As a figure of merit, we take the value of hydrogen evolution rate in the plateau region, which for the particular example in Fig. 8a amounts to 1082, 1218.5,

880 and 88.2 µmol/h for 1 and 10 vol.% of ox-CNT/TiO_2 hybrid, electrospun TiO_2 nanofibres, and TiO_2 nanoparticles, respectively. For reference, normalised per unit mass of catalyst, the data correspond to 34.02, 40.6, 27.66 and to 2.94 mmol/h/g (see more details in Fig. S10). Additionally, experiments of hydrogen production of pure CNTs were performed with similar amounts of photodeposited Pt co-catalyst. We observed negligible photocatalytic activity and therefore we can exclude such effects on photocatalytic performance of our TiO_2/CNT hybrids.

These results demonstrate that electrospun TiO_2 fibres exhibit a remarkable enhancement of H_2 activity with respect to TiO_2 nanoparticles. Amongst key differences between the two materials we point to the synergistic effect of the TiO_2 nanoparticle network in the fibre, facilitating interfacial charge transfer and to the mesoporous structure possibly improving the adsorption and desorption of water photoreduction reactants and products. Similar results have been obtained by electrospinning and calcination of pre-synthesised TiO_2 particles [46], where the observed enhancement in activity was attributed to charge transfer in particle agglomerates, and termed "photo-antennae effect" [47]. The formation of a hybrid of TiO_2/CNTs results in an increase of the H_2 production rate with respect to the TiO_2 fibres of 23 and 38% for 1 and 10vol.% of CNT, respectively, probably by further facilitated electron transfer and mobility across this additional interface [48] and [49].

Our analyses of various hybrid and reference sample materials also show a direct correlation of photocatalytic activity in terms of H_2 evolution rate with increasing fraction of anatase to rutile, plotted in Fig. 8b. We attribute the appreciable variations in the fraction of anatase/rutile in these samples to two factors, namely differences in the actual temperature of the whole material due to the flow of Ar cooling the material and the difficulty in achieving a uniform temperature profile in the large electrospun fibre membranes (which are very good thermal insulators). These variations in phase composition have been very instructive to identify the predominant factors affecting photocatalytic activity (see Table S1 and Fig. S11).

The data in Fig. 8b confirms the much higher activity of electrospun materials compared to nanoparticles, further enhanced by hybridisation with CNTs. This comparison takes into account variations in fraction of anatase-rutile observed in spite of the samples being annealed at the same temperature and same Ar flow. The fact that the hybrids lie on higher line than the pure TiO_2 points to differences in the optoelectronic properties of the materials at the origin of such trends, since a similar anatase-rutile ratio would suggest comparable crystallinity and surface area. From DRS measurements we extract and absorption edge and estimate the band gap for the different types of materials. The band gap turns out to be the same within experimental limits, varying less than 0.1 eV between samples (Fig. S12). However, the presence of surface O vacancies detected by Raman and PL, and suspected to assist the Ti—O octahedral repositioning during phase transformation, changes substantially the surface potential of the materials.

Fig. 9 presents Mott–Schottky plots for the TiO_2 references samples and a hybrid, obtained from EIS in the dark. A positive slope is observed for all the samples, confirming

n-type semiconductor behaviour with electrons as majority carriers. As the slope is inversely proportional to the donor density, the hybrid sample would present the highest donor density possibility due the contribution from the CNTs. More importantly, the flat band potentials estimated from the intercept of the Mott-Schottky plot (Fig. 9) are −0.21, −0.27 and −0.34 V vs. standard hydrogen electrode (SHE) for TiO_2/CNT hybrid fibres, TiO_2 fibres and TiO_2 nanoparticles, respectively. These values correlate well with the photocatalytic activity observed for such samples, as well as their expected oxygen vacancy concentration from Raman spectroscopy.
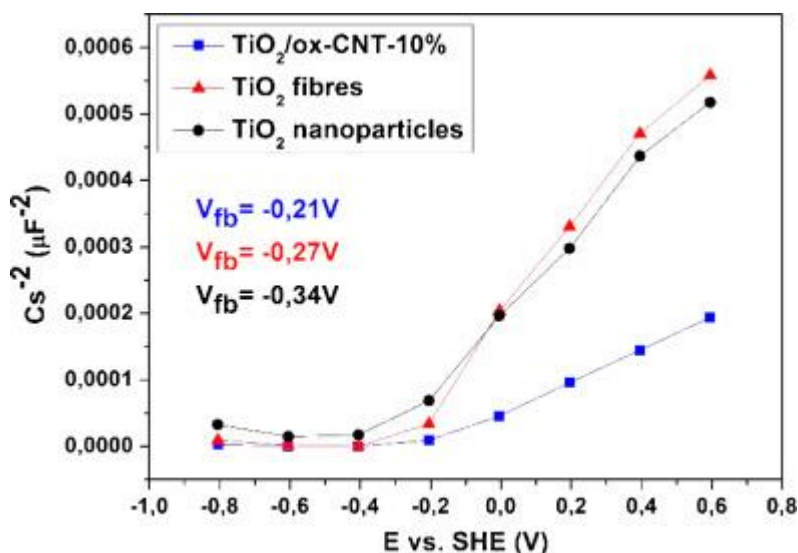

Fig. 9.

Mott–Schottky plot at a frequency of 10 kHz in the dark for electrodes of TiO_2 nanoparticles, fibres and hybrids in 0.1 M Na_2SO_4 aqueous electrolyte.

Figure options

3.6. Comparison of TiO_2-based photocatalysts

Finally, to contextualise the photocatalytic activity values obtained, the data for our hybrids are compared with those reported in the literature. Amongst the vast number of reported values, we have selected only those corresponding to similar photocatalytic hydrogen evolution testing conditions, *i.e.* under UV irradiation, and using Pt as a co-catalyst, and methanol as sacrificial agent. In Fig. 10 we present the comparison of these data against our most active TiO_2 and ox-CNT/TiO_2 hybrid, both in µmol/h.

Fig. 10.
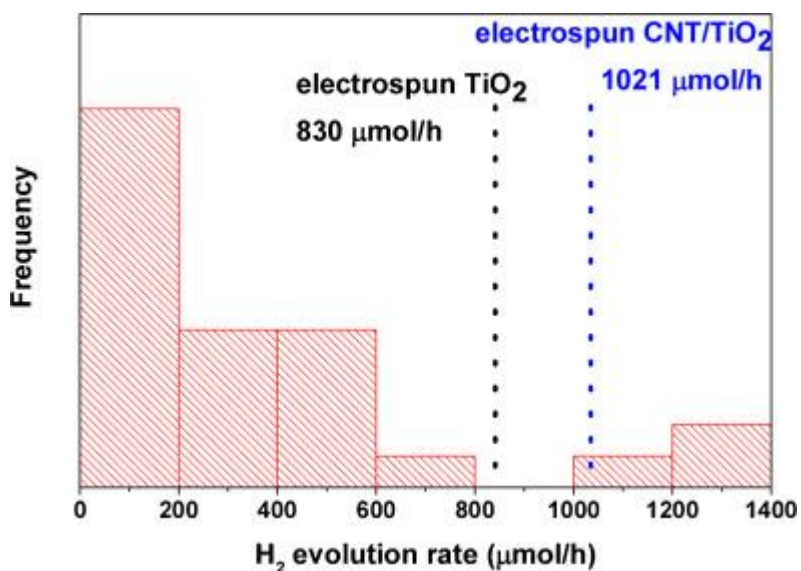
Comparison of photocatalytic efficiency (H_2 evolution rate) of pure TiO_2 fibres and CNT/TiO_2 hybrid fibres in this study compared against data for similar testing conditions. Red bars represent data from literature (see Fig. S13 and Table S2 for details). (For interpretation of the references to colour in this figure legend, the reader is referred to the web version of this article.)

Figure options

We attribute the comparatively high activity of the electrospun samples to three factors: (1) The presence of oxygen vacancies, either on the surface, or at the TiO_2–TiO_2 or TiO_2-CNT interfaces, providing inter-bandgap states and reducing the flat band potential, as discussed above; (2) the catalyst mesoporous structure of interconnected nanocrystals with a large TiO_2–TiO_2 interface to favour charge transfers (thus leading to increased charge lifetimes similar to those reported for other mesoporous TiO_2 photovoltaic devices [41] and photocatalysts [46]); and (3) the presence of CNTs hybridised with TiO_2 nanocrystals in sufficient proximity (<1 nm) to form a metal-semiconductor junction with the CNTs acting as electron acceptors and further contributing to charge separation and increased lifetimes. Future work is directed at determining the electronic structure of the TiO_2/CNT junction, the characterisation of the charge transfer processes through the interfaces between TiO_2/TiO_2 and TiO_2/CNT, and to determine the role of O-vacancy-related inter-bandgap states in such processes.

4. Conclusions

We report on the synthesis and structural characterisation of electrospun CNT/TiO_2 hybrid fibres with remarkably enhanced efficiency for photocatalytic hydrogen production compared with referenced samples. We find interfaces and oxygen vacancies in the materials to play an important role during the structural evolution of the electrospun samples throughout the synthetic route. The polymer used as vehicle for electrospinning

keeps the sol units in close contact, thus resulting in much faster crystallisation caused by a lower activation energy for the nucleation at the interface between particles. Further crystallisation in inert atmosphere to preserve the CNTs results in a non-stoichiometric oxide, in which oxygen vacancies further accelerate crystallisation and the anatase-rutile transformation by Ti—O octahedral repositioning at the interfaces. Thus, electrospun materials have a nanostructure being both continuous and highly porous. This can be visualised as a network of nanocrystals forming large TiO_2/TiO_2 interfaces that facilitates charge transfer and that yields to photocatalytic activity ten times higher than TiO_2 nanoparticles (*i.e.* without electrospinning, and thus lacking interparticle contact and the possibility of internal charge transfers).

The hybridisation with functionalised CNTs produces a further enhancement of photocatalytic activity, which we attribute to the formation of additional TiO_2/CNT interfaces that contribute to spatial charge separation in the material. The combination of advanced spectroscopy techniques (*e.g.* transient absorption, Ultraviolet-XPS) to relate the electronic structure of the hybrids to the charge recombination processes, will help clarify the role of O vacancy-related inter-bandgap states in the hybrids (including a possible Ti—O—C interfacial bond) in charge processes at the CNT/TiO_2 junction and ultimately the photocatalytic activity of the material. This will be the matter of a future study.

Acknowledgements

References

- [1]
- J.H. Im, S.J. Yang, C.H. Yun, C.R. Park
- Nanotechnology, 23 (2012), p. 035604
- [2]
- Y. Zhang, N. Zhang, Z.-R. Tang, Y.-J. Xu
- Phys. Chem. Chem. Phys., 14 (2012), pp. 9167–9175
- [3]
- M.A. Henderson
- Surf. Sci. Rep., 66 (2011), pp. 185–297
- [4]

- S. Muduli, W. Lee, V. Dhas, S. Mujawar, M. Dubey, K. Vijayamohanan, S.-H. Han, S. Ogale
- Acs. Appl. Mater. Interfaces, 1 (2009), pp. 2030–2035
- [5]
- C.J. Shearer, A. Cherevan, D. Eder
- Adv. Mater., 26 (2014), pp. 2295–2318
- [6]
- A.S. Cherevan, P. Gebhardt, C.J. Shearer, M. Matsukawa, K. Domen, D. Eder
- Energy Environ. Sci., 7 (2014), p. 791

[7]

- D. Eder, A.H. Windle
- J. Mater. Chem., 18 (2008), pp. 2036–2043
- [8]
- D. Eder
- Chem. Rev., 110 (2010), pp. 1348–1385
- [9]
- M. Cargnello, M. Grzelczak, B. Rodríguez-González, Z. Syrgiannis, K. Bakhmutsky, V. La Parola, L.M. Liz-Marzán, R.J. Gorte, M. Prato, P. Fornasiero
- J. Am. Chem. Soc., 134 (2012), pp. 11760–11766
- [10]
- M. Krissanasaeranee, S. Wongkasemjit, A.K. Cheetham, D. Eder
- Chem. Phys. Lett., 496 (2010), pp. 133–138
- [11]
- D.M. Guldi, G.M.A. Rahman, V. Sgobba, N.A. Kotov, D. Bonifazi, M. Prato
- J. Am. Chem. Soc., 128 (2006), pp. 2315–2323
- [12]
- J.J. Vilatela, D. Eder
- ChemSusChem, 5 (2012), pp. 456–478

[13]

- G. Zhou, Y. Zhao, C. Zu, A. Manthiram
- Nano Energy, 12 (2015), pp. 240–249
- [14]
- M. Paolucci, F. Marcaccio
- Making and Exploiting Fullerenes, Graphene, and Carbon Nanotubes
- Springer Berlin Heidelberg, Berlin, Heidelberg (2014)
- [15]
- T. Dürkop, S.A. Getty, E. Cobas, M.S. Fuhrer
- Nano Lett., 4 (2003), pp. 35–39
- [16]

- o K.I. Bolotin, K.J. Sikes, Z. Jiang, M. Klima, G. Fudenberg, J. Hone, P. Kim, H.L. Stormer
- o Solid State Commun., 146 (2008), pp. 351–355

  [17]

- o H. Kim, S. Kim, J.-K. Kang, W. Choi
- o J. Catal, 309 (2014), pp. 49–57
- o [18]
- o X.-Y. Zhang, H.-P. Li, X.-L. Cui, Y. Lin
- o J. Mater. Chem., 20 (2010), pp. 2801–2806
- o [19]
- o P. Cheng, Z. Yang, H. Wang, W. Cheng, M. Chen, W. Shangguan, G. Ding
- o Aiche Annu. Meet. Top. Conf. Hydrog. Prod. Storage Spec. (Issue 37) (2012), pp. 2224–2230

  [20]

- o A.S. Cherevan, P. Gebhardt, C.J. Shearer, M. Matsukawa, K. Domen, D. Eder
- o Energy Environ. Sci. (2013)

- o [21]
- o J.-S. Lee, Y.-I. Lee, H. Song, D.-H. Jang, Y.-H. Choa
- o Int. Conf. Electron. Mater. Spec. Issue Iumrs-Icem 2010 Int Conf. Electron. Mater., 11 (2011), pp. S210–S214|
- o [22]
- o X. Wang, M. Xi, F. Zheng, B. Ding, H. Fong, Z. Zhu
- o Nano Energy, 12 (2015), pp. 794–800
- o [23]
- o X. Zhang, P. Suresh Kumar, V. Aravindan, H.H. Liu, J. Sundaramurthy, S.G. Mhaisalkar, H.M. Duong, S. Ramakrishna, S. Madhavi
- o J. Phys. Chem. C, 116 (2012), pp. 14780–14788
- o [24]
- o H. Jamil, S.S. Batool, Z. Imran, M. Usman, M.A. Rafiq, M. Willander, M.M. Hassan
- o Ceram. Int., 38 (2012), pp. 2437–2441
- o [25]
- o D. Tasis, N. Tagmatarchis, A. Bianco, M. Prato
- o Chem. Rev., 106 (2006), pp. 1105–1136
- o [26]
- o A.L. Patterson
- o Phys Rev, 56 (1939), pp. 978–982
- o [27]
- o R.A. Spurr, H. Myers

- Anal. Chem., 29 (1957), pp. 760–762
- [28]
- S. Aksel, D. Eder
- J. Mater. Chem., 20 (2010), p. 9149
- [29]
- P.S. Kumar, S.A.S. Nizar, J. Sundaramurthy, P. Ragupathy, V. Thavasi, S.G. Mhaisalkar, S. Ramakrishna
- J. Mater. Chem., 21 (2011), pp. 9784–9790
- [30]
- C.J. Brinker
- Sol–gel Science: The Physics and Chemistry of Sol–gel Processing
- Academic Press, Boston (1990)
- [31]
- K.-R. Zhu, M.-S. Zhang, Q. Chen, Z. Yin
- Phys. Lett., 340 (2005), pp. 220–227
- [32]
- D. Eder, M.S. Motta, A.H. Windle
- Acta Mater., 58 (2010), pp. 4406–4413
- [33]
- P. Docampo, M. Stefik, S. Guldin, R. Gunning, N.A. Yufa, N. Cai, P. Wang, U. Steiner, U. Wiesner, H.J. Snaith
- Adv. Energy Mater., 2 (2012), pp. 676–682
- [34]
- J. Liqiang, Q. Yichun, W. Baiqi, L. Shudan, J. Baojiang, Y. Libin, F. Wei, F. Honggang, S. Jiazhong
- Sol. Energy Mater. Sol. Cells, 90 (2006), pp. 1773–1787
- [35]
- D. Pan, N. Zhao, Q. Wang, S. Jiang, X. Ji, L. An
- Adv. Mater., 17 (2005), pp. 1991–1995
- [36]
- L. Collado, P. Jana, B. Sierra, J.M. Coronado, P. Pizarro, D.P. Serrano, V.A. de la Peña O'Shea
- 7th Eur. Meet. Sol. Chem. Photocatal. Environ. Appl. Spea 7, 224 (2013), pp. 128–135
- [37]
- L. Collado, A. Reynal, J.M. Coronado, D.P. Serrano, J.R. Durrant, V.A. de la Peña O'Shea
- Appl. Catal. B Environ. (2015) (in press)
- [38]
- T. Berger, D. Monllor-Satoca, M. Jankulovska, T. Lana-Villarreal, R. Gómez
- ChemPhysChem, 13 (2012), pp. 2824–2875
- [39]
- J.M.G. Amores, V.S. Escribano, G. Busca
- J. Mater. Chem., 5 (1995), p. 1245
- [40]

- o H. Zhang, J. Banfield
- o Am. Miner, 84 (1999), pp. 528–535

- o [41]
- o S. Nakade, M. Matsuda, S. Kambe, Y. Saito, T. Kitamura, T. Sakata, Y. Wada, H. Mori, S. Yanagida
- o J. Phys. Chem. B, 106 (2002), pp. 10004–10010
- o [42]
- o D.A.H. Hanaor, C.C. Sorrell
- o J. Mater. Sci., 46 (2011), pp. 855–874
- o [43]
- o D. Eder, A.H. Windle
- o Adv. Mater., 20 (2008), pp. 1787–1793
- o [44]
- o R. Urlaub, U. Posset, R. Thull
- o J. Non-Cryst. Solids, 265 (2000), pp. 276–284
- o [45]
- o K.S. Finnie, V. Luca, P.D. Moran, J.R. Bartlett, J.L. Woolfrey
- o J. Mater. Chem., 10 (2000), pp. 409–418
- o [46]
- o S.K. Choi, S. Kim, S.K. Lim, H. Park
- o J. Phys. Chem. C, 114 (2010), pp. 16475–16480
- o [47]
- o Y. Park, W. Kim, D. Monllor-Satoca, T. Tachikawa, T. Majima, W. Choi
- o J. Phys. Chem. Lett., 4 (2013), pp. 189–194
- o [48]
- o T. An, J. Chen, X. Nie, G. Li, H. Zhang, X. Liu, H. Zhao
- o Acs Appl. Mater. Interfaces, 4 (2012), pp. 5988–599
- o [49]
- o X. Pan, Y. Zhao, S. Liu, C.L. Korzeniewski, S. Wang, Z. Fan
- o ACS Appl. Mater. Interfaces, 4 (2012), pp. 3944–3950